



ELSEVIER

Contents lists available at SciVerse ScienceDirect

Journal of the Mechanics and Physics of Solids

journal homepage: www.elsevier.com/locate/jmps

Mapping forces in a 3D elastic assembly of grains

Mohammad Saadatfar^{a,*}, Adrian P. Sheppard^a, Tim J. Senden^a, Alexandre J. Kabla^{b,**}^a Research School of Physics and Engineering, The Australian National University, Canberra ACT 0200, Australia^b Department of Engineering, University of Cambridge, Trumpington Street, CB2 1PZ Cambridge, UK

ARTICLE INFO

Article history:

Received 26 February 2011

Received in revised form

29 September 2011

Accepted 2 October 2011

Available online 6 October 2011

Keywords:

Granular matter

Force measurement

3D image processing

Tomography

Segmentation

ABSTRACT

Our understanding of the elasticity and rheology of disordered materials, such as granular piles, foams, emulsions or dense suspensions relies on improving experimental tools to characterise their behaviour at the particle scale. While 2D observations are now routinely carried out in laboratories, 3D measurements remain a challenge. In this paper, we use a simple model system, a packing of soft elastic spheres, to illustrate the capability of X-ray microtomography to characterise the internal structure and local behaviour of granular systems. Image analysis techniques can resolve grain positions, shapes and contact areas; this is used to investigate the material's microstructure and its evolution upon strain. In addition to morphological measurements, we develop a technique to quantify contact forces and estimate the internal stress tensor. As will be illustrated in this paper, this opens the door to a broad array of static and dynamical measurements in 3D disordered systems.

Crown Copyright © 2011 Published by Elsevier Ltd. All rights reserved.

1. Introduction

Despite the practical importance of macroscopic disordered materials such as soil, foams and emulsions the rules that govern their mechanical behaviour remain poorly understood. In the case of granular materials, these studies are essential to the advancement of related industrial processes and also to the prediction of often catastrophic geological phenomena (avalanches of slurries, earthquakes). Although empirical constitutive equations are nowadays able to partly model the response of these systems, a unified multiscale framework does not exist yet. Over the past 20 years, foams and granular systems have emerged as a model system for low temperature glasses (Langer and Liu, 2000). Many theories (Falk and Langer, 1998; Zhang and Makse, 2005; O'Hern et al., 2001), simulations (Lemaître, 2002) and experiments (Utter and Behringer, 2008) have been designed to address the relationship between the internal structure and macroscopic behaviour of such systems. The overall effective mechanical properties of granular systems is intricately entangled with the complex nature of interactions between their constituent particles. Consequently many studies attempt to use complex models that account for elastoplastic deformation and non-affine displacement at the grain scale to bridge between micro- and macro-scale (Falk and Langer, 1998; Lemaître, 2002; Majmudar and Behringer, 2005; Utter and Behringer, 2008). Some of these theories and models often use approaches derived from statistical physics. Although the behaviour of foams seems today rather well understood (Weaire et al., 2010), the complexity of granular matters behaviour at the microscopic scale has prevented a proper physical model of granular systems.

* Corresponding author. Fax: +61 2 61250732.

** Corresponding author. Fax: +44 1223 3 32662.

E-mail addresses: mos110@physics.anu.edu.au (M. Saadatfar), ajk61@cam.ac.uk (A.J. Kabla).

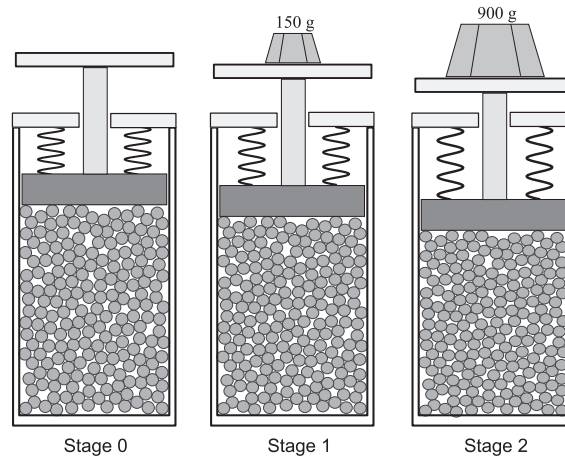


Fig. 1. Sketch of the compression cell and consecutive stages of compression.

A large part of the problem arises from the strongly nonlinear contact law between rigid bodies coupled with the dynamical nature of the contact network. In this context, the spatial distribution and temporal evolution of the force network has become a highly sought after quantity that expands from micro-scale (grain–grain contacts) to macro-scale (granular assembly).

Early simulations have provided important insights on the internal force distributions of a granular pile (Radjai et al., 1996; Coppersmith et al., 1996; Makse et al., 2000). Two-dimensional (2D) experiments managed to keep up with the pace of advancement in simulations (Drescher and de Josselin de Jong, 1972; Howell et al., 1999; Kolb et al., 2004; Zhang et al., 2010), 3D experiments, however, have been limited to measurements of the distribution of forces only at the boundaries of the containers (Brockbank et al., 1997; Mueth et al., 1998; Blair et al., 2001; Corwin et al., 2005). These experimental methods could not have access to the spatial arrangement of the contact force network in the bulk of granular assembly. Moreover they were unable to determine structural features such as force chains and arching which have been postulated as the signature of jamming (Lois and Carlson, 2007).

In recent years, a range of tools have been developed to apprehend the 3D nature of bulk properties. X-ray or MRI techniques have allowed to study dynamic properties of granular systems such as flow profiles and shear banding, at a mesoscopic scale (Mantle et al., 2001; Kabla et al., 2005; Kabla and Senden, 2009; Dijkstra and van Hecke, 2010). 3D reconstructions of compressed emulsion systems using confocal microscopy have provided the first measurements of the bulk force distributions (Brujić et al., 2003, 2005) by estimating the contact force from contact geometry. A similar technique has also been used to characterise spatial correlations of forces inside 3D piles of frictionless liquid droplets (Zhou et al., 2006). Although these observations are very valuable, the systems used are significantly different from real granular pile which has different contact laws and frictional properties.

X-ray computed tomography has been used for static characterisation of large packings of spherical grains (Silbert et al., 2002; Aste et al., 2005; Saadatfar, 2006). In this study, we apply this technique to a model system made of soft millimetric elastic beads. In addition to the measurement of traditional structural quantities (packing fraction, coordination number, etc.), the contact force is measured from the contact area between grains which can be integrated at a mesoscopic scale to estimate the local stress tensor in the pile. We then apply a series of external forces to our model system and investigate its response to these stress controlled loadings. The experiment combined with imaging and image analysis as well as microstructural and micromechanical characterisation provide an all-in-one methodology that allows probing into complex systems such as granular assemblies. This approach delivers results consistent with the existing literature and is promising as a generic tool to study the local, nonlinear mechanics of granular assemblies.

2. Experiment and methodology

2.1. Experimental setup

The packing studied in this paper is made of relatively monodisperse spherical rubber balls of diameter 3.10 ± 0.05 mm. The grains are made of commercial rubber¹ with a shear modulus estimated at 850 kPa.

A cylindrical PMMA container, with internal diameter of 44 mm is used as a compression cell (see Fig. 1). The inner wall of the cylinder is lubricated with canola oil to reduce the friction. Two thousand and twenty rubber elastic balls are then poured into this chamber. The latter is then closed at the top by a piston of diameter slightly smaller than the container; it

¹ Styrene-Butadiene-Rubber (SBR); purchases from Mid-Atlantic Rubber Co., USA.

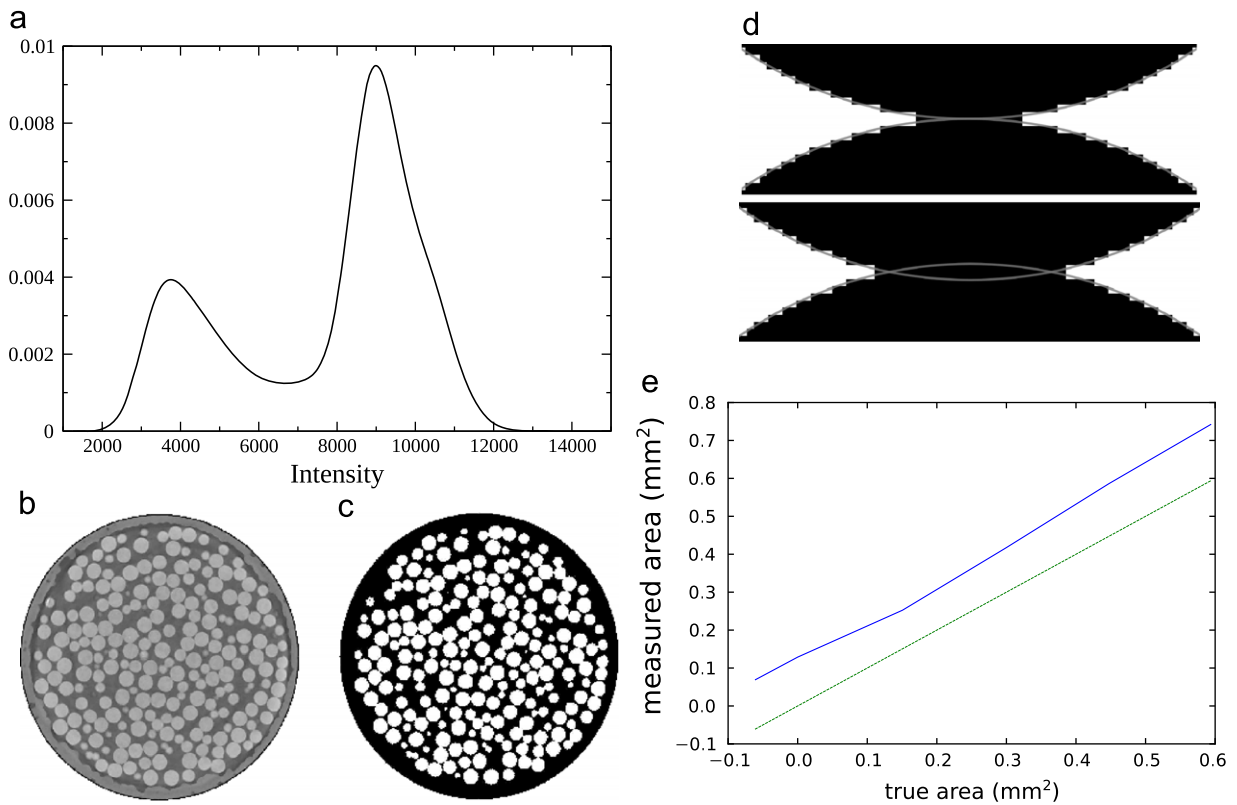


Fig. 2. (a) Normalised X-ray density histogram of the full image volume of the rubber ball sample. (b) Gray scale X-ray density map of a slice of rubber ball sample. (c) The same slices after phase separation. (d) Illustration of the effect of segmentation process on grain contact area. Cross section of two binarised computer generated images with the same resolution as grains in this study (115 pixels in diameter). Top image: the grains when they are just touching. Bottom image: the grains have a small overlap (penetration is 1% of the grain diameter). (e) Measured contact area on the computer generated binarised images as a function of true contact area for a range of grain overlaps.

can therefore move freely without touching the PMMA cylinder and without allowing beads to leave the container. A horizontal platform is rigidly connected by a shaft to the piston so that a load can be applied to the sample by placing weights on it. A pair of springs connecting the piston to the container is used to make sure that, in the absence of a load, the piston does not fall down due to its own weight.

The compression cell is attached to a motorised rotation stage located between a high-resolution microfocus X-ray source (80 kV accelerating voltage and 200 μ A beam current and a CCD detector of the size 67 mm \times 67 mm, 2048 \times 2048 pixels of size 33.6 μ m each (Sakellariou et al., 2004a,b). The compression cell is rotated by about 0.125° increments around its vertical axis and a radiographic projection of the packing is taken after each rotation with an exposure time of 18 s. A total of 2880 projections are taken for a complete rotation of the specimen. It takes approximately 15 h to scan the volume for each case. After the completion of each scan, tomographic cone beam reconstructions are performed on these 2880 projections using the (Feldkamp et al., 1984) algorithm. Tomograms of about 2000³ voxels are obtained at 27 μ m resolutions.

We have recorded and analysed the internal geometry of the packing under three different loading conditions.

Stage0: Pre-compression stage with no extra loading; the piston is held in balance just above the top of the packing without making contact with it (see Fig. 1). Rubber balls are at rest, only bearing their own weight (41.1 g). The combined weight of the piston and the platform (600 g) is fully balanced by the pull of the springs so that at this point there is no external force being exerted onto the pile.

Stage1: The platform is loaded with 150 g (1.47 N). By taking into account the opposite force applied by the springs, a net weight of 115 g is applied to the packing, resulting in a compressive strain of $\varepsilon = 3.78\%$. We define the axial strains as the ratio of the displacement of piston to the initial height of the packing (engineering strains).

Stage2: A total of 900 g (8.83 N) is placed on the platform resulting in a net 780 g weight on the packing. The total axial strain at that stage is $\varepsilon = 7.83\%$.

2.2. 3D image analysis: segmentation and partitioning

The tomographic image consists of a cubic array of reconstructed linear X-ray attenuation coefficient values, each corresponding to a finite volume cube (voxel) of the sample. The first step in analysing this data is to differentiate the

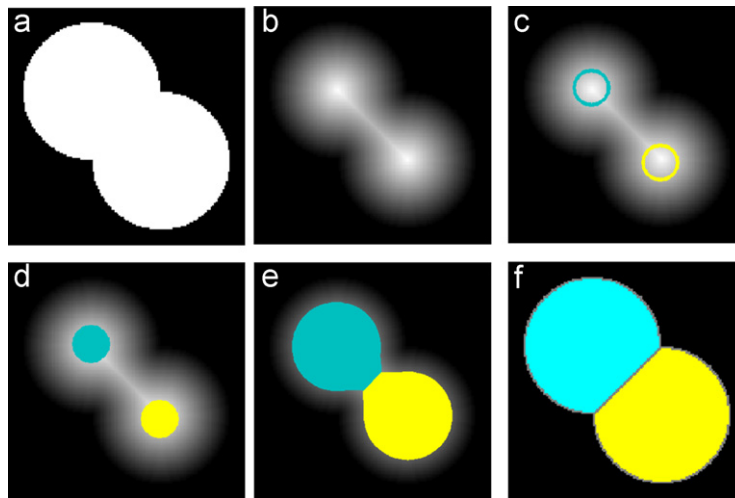


Fig. 3. Different stages of the watershed algorithm. (a) Two overlapping discs. (b) EDT of the two overlapping discs. (c) Identifying the local maxima (seeds). (d) Region growing from the identified seeds. (e) Further growth of the regions along the Euclidean distance map by having pixels on their boundary added to them. The growth continues until neighbouring regions begin to touch. (f) Discs separated.

attenuation map into distinct pore and grain phases. Ideally, one would wish to have a bi-modal distribution giving unambiguous phase separation of the pore and solid phase peaks. This simple phase extraction is possible in our rubber ball pack. The intensity histogram of the tomogram (Fig. 2(a)) shows two distinct peaks associated with the two phases (beads and air). The peak centred around 9000 is associated with the beads and the lower peak around 4000 is associated with the pore phase.

The segmentation algorithm (Sheppard et al., 2004) uses both the attenuation value and its gradient to detect interfaces between the two phases (grain-void). In order to detect an interface, a sharp gradient of attenuation is required. This method, after adjustment (Saadatfar et al., 2006), provides a very robust detection of grain boundaries, but it only works if the void spaces is larger than one voxel size. In particular, if the gap between two grains is very small (order of a voxel or less), the density gradient across the gap between these two grains will not appear as steep as a typical grain-void interface. This can result in the detection of false contact regions in the segmented datasets which consequently gives rise to the following undesired morphological effects: (i) detection of false contacts between grains, and (ii) the surface area of real contacts can appear larger than their actual values. These types of segmentation errors are illustrated in Fig. 2(d). Using computer generated images of contacting spheres binarised at the resolution used in this study (115 pixels in diameter), we find that segmentation errors lead to a contact offset on the apparent contact area (see Fig. 2(e)). Although the tomogram resolution is consistent with the physical resolution of the instrument and number of projections taken, we nevertheless expect to have a slightly larger shift in the real data compared to perfectly contrasted computer generated images. As detailed later in this paper, this offset in surface area can be corrected using a mechanical calibration.

The next step is to reconstruct and label individual grains from the geometry of the solid phase. The basic assumption in the grain identification algorithm is that the boundaries between grains which are not isolated coincide with the watershed surfaces of the Euclidean distance map of grains (distance to the nearest grain boundary) (Vincent and Soille, 1991). The entire grain space can be thought of as the union of spheres centred on every grain voxel. Each sphere radius is given by the Euclidean distance value of the voxel at its centre. The next stage is identifying all the voxels that are not covered by any larger Euclidean spheres.

Each one of these voxels, which are at the maxima of the distance function in their local neighbourhood, then forms a seed that will grow into a single grain in the following stage of the algorithm. Fig. 3 illustrates a simple 2D case where two overlapping discs are separated. The seed regions essentially grow by having voxels on their boundary added to them. Voxels that lie on the boundaries of the regions are processed in reverse Euclidean distance order, i.e. voxels with high distance values are processed first. When a voxel is processed, it is assigned to the region on whose boundary it lies, or, if it lies on more than one region boundary, the region whose boundary it first became part of. At the end of the algorithm, the grain space will be partitioned into grains whose boundaries lie on the watershed surfaces of the Euclidean distance function (Saadatfar, 2006). The watershed based grain partitioning algorithm is computationally expensive. Hence it is parallelised (using an implementation of the “time warp” discrete event simulation protocol, (Soille, 2003)), so it can be used to analyse very large datasets ($\sim 2000^3$).

3. Measurements

The 3D watershed algorithm provides us with large amounts of information about the pile structure. Each grain has been labelled, its location and shape are known, its direct neighbours have been identified, and the geometry of the contact

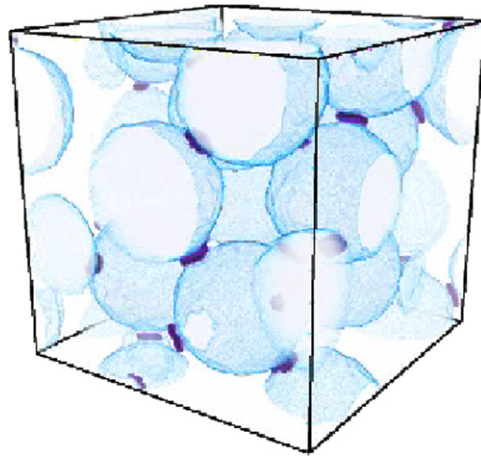


Fig. 4. A sub-volume of the elastic ball compaction experiment. The contact zone between touching grains (dark patches) provides a measurement of contact force.

Table 1
Details of the compression progression.

Compression stage	0	1	2
External loading (g)	0	115	780
Avg. vertical stress (σ_{zz}) for top 1/3 of packing (Pa)	578	1021	4937
Strain (%)	0	3.78	7.83
Packing fraction	0.57	0.59	0.62
Avg. coord. no. raw	6.28 ± 1.64	6.63 ± 1.58	7.13 ± 1.49
Avg. coord. no. filtered	4.99 ± 1.80	5.32 ± 1.66	5.92 ± 1.56

they share can be extracted as well. This data can now be processed to extract physical and mechanical properties. In this section, we present a few methods implemented in the context of granular systems. These can be separated into structural characteristics and mechanical measurements. The latter involves kinematic and force measurements that rely on prior knowledge of a contact law for individual grains.

3.1. Structural quantities

3.1.1. Packing fraction

One of the most readily measurable quantities from 3D images is the packing fraction. Packing fraction or apparent density is defined as the ratio of the volume of balls to the total volume. Table 1 summarises the packing fractions measured directly from the digital images. The packing fractions we measure on the initial pile is 57%, which is in the lower end of the spectrum for monodisperse beads. Such a density is achievable in our system due to the large frictional coefficient of rubber–rubber contacts. As the loading is increased, the volume fraction increases up to 62%.

3.1.2. Radial distribution function

From the shapes of the individual grains calculated by the Watershed algorithm, the coordinates of each grain's centre of mass can be accurately measured. This data is in particular required to characterise the microstructure of granular systems and to calculate the autocorrelation function of the grain centres.

The radial distribution function (RDF) is a measure of the degree of separation of grain centres and their density at a given distance. It is calculated by counting the number of grains N that are separated from a given sphere by a distance in the interval $[r, r+dr]$, where r is the distance between grain centres. For large r , the RDF represents the random spatial structure of the packing and the number density of the grain centres found in the interval $[r, r+dr]$ approaches the average density of grains in the packing, $(3/4\pi R^3)\rho$, where ρ is the packing fraction and R is the average grain radius. In our calculations, we normalise RDF by the average density, therefore for large r the RDF approaches unity. Fig. 5 shows the RDF in our packings throughout compression progression. The RDF of the system before insertion of any external force (stage 0) shows a prominent peak at $r \approx D_g$ where D_g is the average grain diameter ($D_g = 2 \times R \approx 3 \times 10$ mm). The second peak appears at $r \approx 1.95D_g$ and a sub-peak approximately at $r = \sqrt{3}D_g$. As the vertical load increases (stages 1 and 2), the peaks of the RDF slightly widen and shift to the left due to the compression of touching spheres, hence shortening the centre–centre distance between them (see Fig. 5(left)).

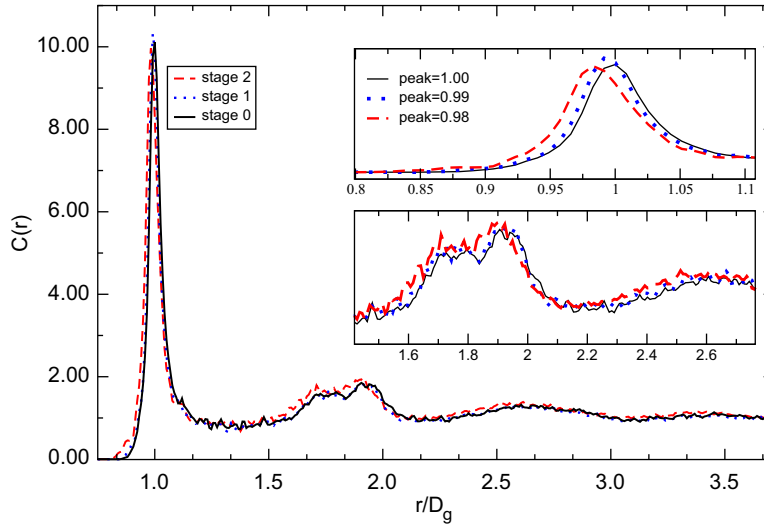


Fig. 5. Radial distribution function of the packing at different stages of compression normalised by the volume of a single grain and the packing fraction. Note the shift in the peaks as the pressure increases.

We have compared the width of the sub-peaks around $r = \sqrt{3}D_g$ and $1.95D_g$ with previous experiment (Aste et al., 2005) and simulations (Martin and Bordia, 2008) of hard sphere packing. The comparison reveals that the peaks in our RDF are wider than their equivalent in these studies. This is due to the fact that grains in our experiment are deformable, and therefore the geometry of local tetrahedral configuration is not as constrained as it is in the case of hard sphere packing. Another contributing factor is related to the relatively low packing fraction of our granular assembly which is mainly due to high friction between rubber balls. As a result of this low packing fraction, the packing structure tends to be more disordered. As a result, the local structural motifs are not as pronounced as high density packings of hard spheres. It is noteworthy that in our calculations of RDF, we exclude the boundary grains therefore removing the effect of highly ordered border grains.

The magnitude of the shift is about 1% and 2% for stages 1 and 2. This is to be compared with the macroscopic axial strain which is of the order of 4% and 8% without any deformation along the order directions. This suggests that the internal compression is more isotropic than the loading.

3.1.3. Mean coordination

The grain partitioning also provides us with the list of contact areas between grains, from which it is possible to analyse the contact network of grains. Using first the raw data from the watershed algorithm, we have measured the coordination (number of contacts) of each grain and plotted its distribution for each stage of compression (see Fig. 6(a)). This plot shows a significant increase of grain coordination as the loading increases. It is notable that as pressure increases, the distributions move to higher values and get slightly narrower (see Table 1). This increase in the coordination number is achieved by re-organisation of grains in the packing when they are compressed and also grain compression/deformation process which reduces the overall grain–grain distance. A relatively large number of grains lose their contacts with some of their immediate neighbours while almost the same amount gain new contacts as the compression progresses. We have shown the histogram of lost/gained contacts in the inset of Fig. 6. Negative values on the horizontal axis represent lost contacts while positive values show the number of newly gained contacts. Nearly 50% of grains retain their coordination number during the compression without any changes.

As discussed in Section 2.2, the inherent finite resolution of the CT leads to systematic bias in fine details such as grain contacts (Marmottant et al., 2008); if the gap between two grains is in the order of, or less than, the voxel size, grains will appear to be in contact in the segmented data. To correct for this intrinsic resolution limitation, we offset all the contact areas by a small amount, which essentially corresponds to the apparent contact area of two touching perfectly spherical grains (see Section 3.2.3 for detailed discussion). All contacts whose apparent surface area is below this threshold, are therefore discarded. Fig. 6(b) shows a re-plot of Fig. 6(a) after applying the offset. The isostatic limit for mechanically stable packing of spheres in 3D suggests a connectivity of 4 for frictional and 6 for frictionless systems. In our measurements, the average coordination number is ≈ 5 for stage 0 (see Fig. 6(b)) which is in agreement with previous measurements (Bernal and Mason, 1960; Aste et al., 2005).

3.2. Kinematics and dynamics

3.2.1. Displacement fields

Next we calculate the coordinates of the centroid of the grains for all three scans and then track each individual grain throughout the experiment. As an illustration, we render the 3D vector field derived from tracking grains during the compression for both stages of compression, see Fig. 7(a, b).

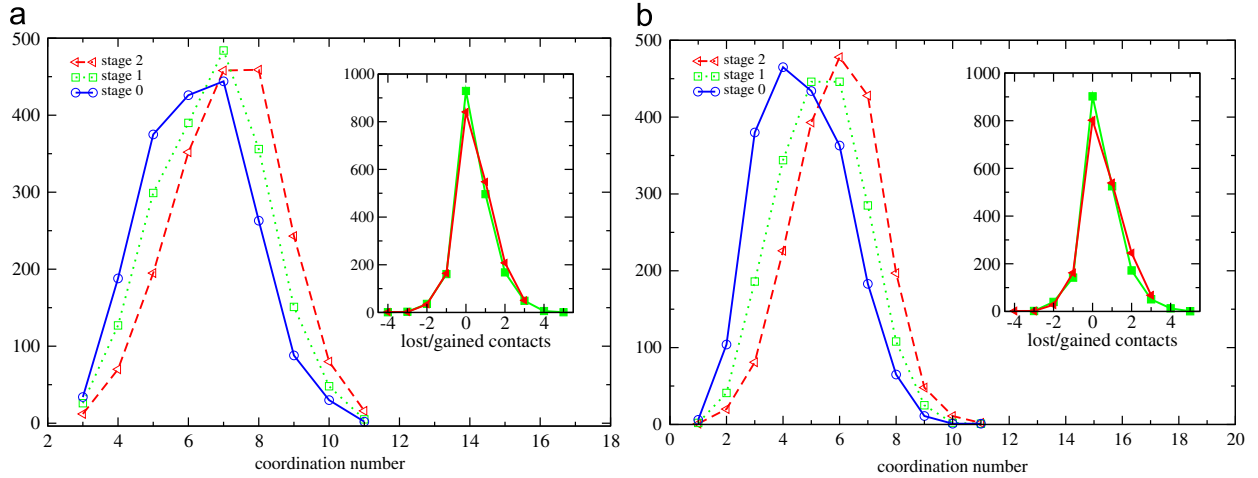


Fig. 6. Histogram of coordination number as a function of loading for different threshold values: (a) No threshold is applied (using the raw data after watershed algorithm). (b) After a threshold value of 0.25 mm^2 is subtracted from all contact surface areas. As a result the average coordination number is reduced in all three stages.

To gain a qualitative insight into the displacement field, we measure the average displacement of grain centres in both longitudinal and radial directions. Fig. 8(a) demonstrates such displacement along the loading axis. As expected, gradient of displacement from top to bottom shows that the system is under vertical compression. The decrease of the slope with depth also indicates that part of this stress is screened by the time it reaches the bottom. A standard explanation of this is the Janssen effect (Janssen and Zeitschr, 1895), suggesting that friction on the lateral walls might be significant. To confirm this, we studied the vertical displacement profile in the radial direction (Fig. 8(b)) which confirms that grain movements closer to the outer region of cylinder are smaller than that of the central region. Therefore a shear component in the (z, r) direction is expected. Another feature of the displacement field is the weak but noticeable radial displacement of the grain towards the boundary (see Fig. 8(c)). This radial displacement can be clearly seen in Fig. 7(a).

3.2.2. Contact mechanics

In addition to the direct measurement of individual grain displacements, a number of other mechanically relevant features can be extracted from the tomogram. Upon compression, we observed that the distance between grains varies, as well as shape and contact areas between them. These quantities can *a priori* be used to quantify the force transmitted between the grains. In this section, we describe the implementation of a contact model that is suitable for stress calculations from 3D images.

Contact mechanics between solid objects have been studied for over a century. The seminal works of Hertz (1882) and Mindlin (1949) about the contact mechanics of solid bodies have provided analytical solutions for idealised cases, summarised in Johnson (1987). The contact force between two elastic spheres can be calculated from the nonlinear Hertz–Mindlin model. The expression of the normal force between two contacting elastic spherical grains m and n with

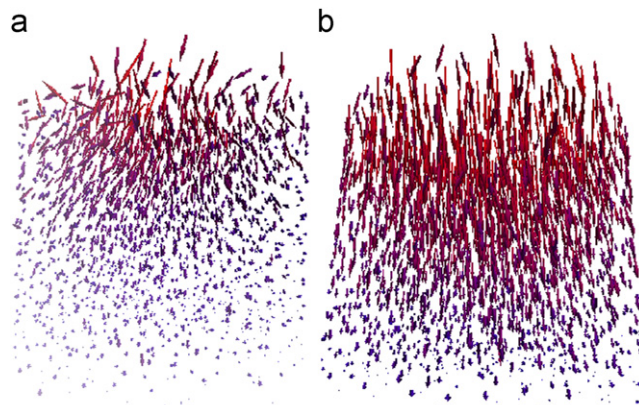


Fig. 7. Displacement field presented as vector fields (velocity fields) for stage 1 (a) and 2 (b) of the experiment.

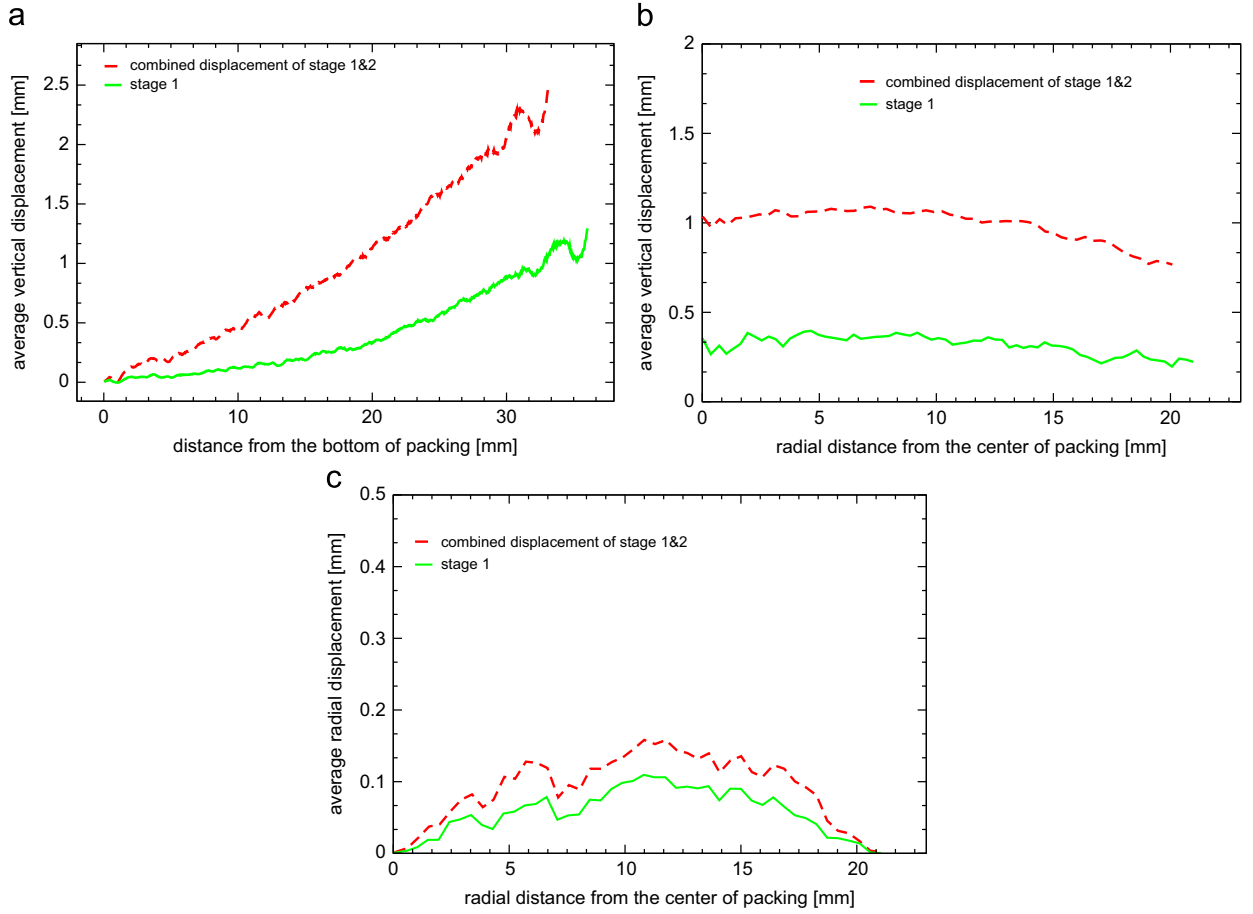


Fig. 8. Displacement field along the loading axis. (a) The overall vertical displacement field is represented very well by an exponential equation. For visual convenience every 30 data points is shown. (b) Longitudinal displacement for the 1st stage and the overall displacement. Here we choose a bin size of 0.4 mm for averaging. (c) Average radial displacement of grains measured from the distance between the centre of packing its outer boundary.

uncompressed radii R_m and R_n , made of the same material, is given by

$$f_{mn} = \frac{2}{3} \frac{4G}{1-\nu} R^{1/2} \zeta_{mn}^{3/2}, \quad (1)$$

where R is the geometric mean of R_m and R_n , $R = 2R_m R_n / (R_m + R_n)$, ζ_{mn} is the normal overlap, or penetration length, as depicted in Fig. 9a, G is the shear modulus and ν the Poisson ratio of the grains, equal to 0.5 for rubber (Zhang and Makse, 2005).

We have tested the mechanical response of our grains by compressing a few individual grains between two steel plates and measuring the force required as a function of the gap between the plates (Fig. 9). The response of the grains is consistent with the Hertz model, and we have extracted from these graphs the value of the grains shear modulus, 850 kPa, which is a reasonable value for a commercial rubber.

The Hertz–Mindlin theory therefore provides us with a suitable model to calculate the contact force from the grain geometry, as long as we have a good estimate of the normal overlap ζ for each contact. Two options can be considered at this stage. (i) The normal overlap can be estimated from the distance between grain centres. If the grains are located at positions \mathbf{r}_m and \mathbf{r}_n , assuming grains remain spherical, $\zeta_{mn} = \frac{1}{2}[R_m + R_n - |\mathbf{r}_m - \mathbf{r}_n|]$. The autocorrelation function shows that we expect this quantity to be of the order of a few percent of the grain diameter. Although the grain location is determined accurately, calculation of ζ can be fairly inaccurate due to the anisotropy of the imposed strain causing the grains to deviate significantly from a spherical shape into more ellipsoidal geometries. The centre–centre distance is therefore not a good approach to estimate the contact geometry. (ii) Our image processing protocols deliver a sensitive measurement of the contact area (Fig. 4), which provides us with a more reliable method to calculate the forces independently of the centre–centre distances. The contact area (s_{mn}), between grains labelled by m and n , is related with the normal overlap ζ_{mn} by

$$\zeta_{mn} = \frac{s_{mn}}{2\pi R}. \quad (2)$$

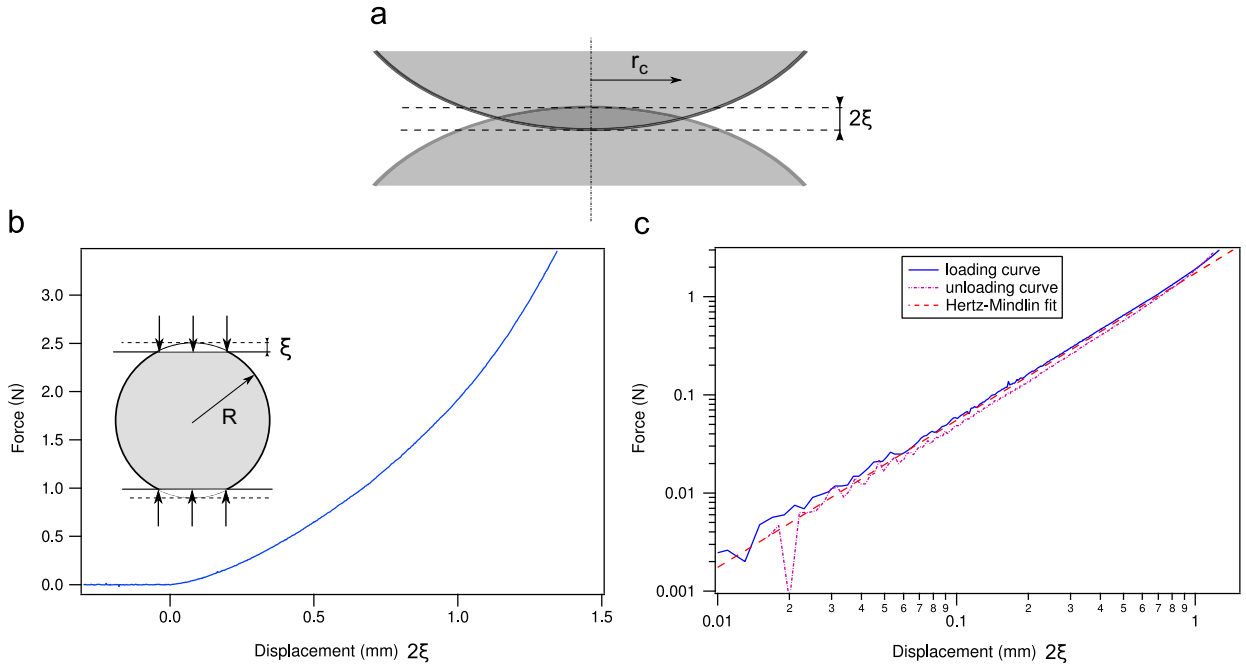


Fig. 9. Response of a single rubber ball to loading.

This purely local measurement of the force can be applied to any grain geometry, as long as the local curvature of the grain near the contact point can be estimated as well.

3.2.3. Force distribution and stress field

As illustrated in Fig. 2(e), the finite resolution of the CT causes a systematic increase of the contact areas that needs to be carefully compensated for. Essentially, two surfaces will appear in contact if they are separated by less than a distance δ , depending on the instrument precision but typically of the order of the voxel size. Assuming that the grains look $\delta/2$ larger than what they actually are, the corresponding effect on the contact area is, according to formula 2, a simple additive offset $s_{off} = \pi R\delta$, consistent with Fig. 2(e). However, even if we estimate δ to be of the order of a voxel, obtaining a more accurate value is important and requires an additional calibration of our measurements.

The mean stress in the vertical direction at the vicinity of the upper interface can be estimated in two independent ways for each loading step; either from the knowledge of the loading mass and geometry of the setup or by using the contact forces to calculate the stress tensor in the bulk of the pile. We consider a sub-volume δv of the size $4 \text{ mm} \times 4 \text{ mm} \times 12 \text{ mm}$ containing ≈ 13 grains. Each contact contained in this volume bears a force denoted \underline{f}_{mn} , measured from the contact area s_{mn} between grains indexed by m and n . The centre to centre vector is noted $\underline{l}_{m,n}$. The components of the stress tensor, indexed by i and j , are then obtained from the following expression (Thornton and Antony, 1998):

$$\sigma_{ij} = \frac{1}{\delta v} \sum_{m,n} f_{mn}^i l_{mn}^j, \quad (3)$$

where the sum is over all contacting pairs of grains in the volume δv .

In order to measure the contact area offset s_{off} required to compensate for the segmentation error, we have calculated, using the upper third of the sample, the mean vertical stress σ_{zz} we would obtain for a range of values of s_{off} (Fig. 10). A suitable choice should provide the value of the normal stress consistent with the loading applied on the sample (i.e. where the solid line intersects the dotted line in Fig. 10). Based on this graph, we find that a good choice of surface offset is between 0.2 mm^2 and 0.3 mm^2 , and select $s_{off} = 0.25 \text{ mm}^2$ in what follows. This value provides a reasonable reading of the normal stress for the highest load value (stage 2), for which the calibration is the most reliable due to the large values of the force and increased number of contacts (see Table 1). For stage 0, the overall mean stress appears however to be overestimated for any reasonable values of the offset. The contact area offset is, as expected, larger than but comparable with the estimate obtained from computer generated data (see Fig. 2(e)). Using formula (2), we find that this value corresponds to an additional overlap $\delta/2 = 0.02 \text{ mm}$, consistent with the size of a single voxel.

Once this tool is calibrated, it can be used to probe a number of statistical quantities in the pile. Fig. 11 shows the distribution of normal forces in the pile for the three different loads studied here. The 3D bulk measurement of the contact normal forces exhibit a number of features that are characteristic of granular systems. In particular, a salient feature of

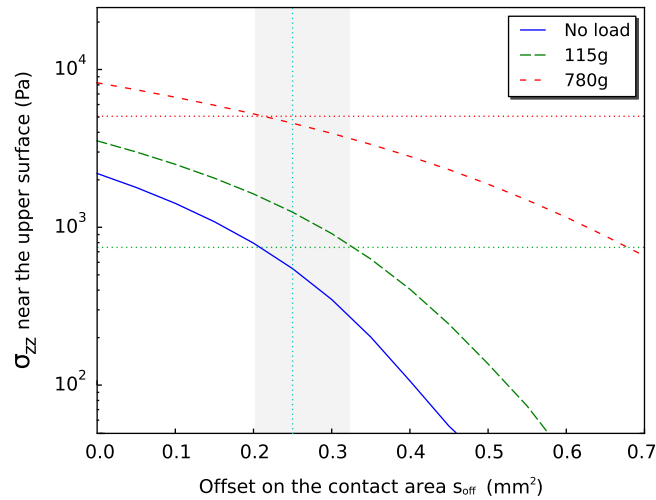


Fig. 10. Solid lines: the mean vertical stress as a function of contact area offset. Dotted lines: the applied load, 740 Pa for stage 1, and 5000 Pa for stage 2 (see Table 1).

force measurement presented in this study is that the distributions are primarily exponential for large forces. This is in agreement with earlier measurements in 2D piles (Coppersmith, 1997; Liu et al., 1995) or at a 3D interface (Brujić et al., 2005) and also the numerical studies of dynamics of granulated systems (Radjai et al., 1996). Another feature often reported in granular dynamics studies (O'Hern et al., 2001; Majmudar and Behringer, 2005) is the presence of a peak or a plateau at low forces. However, this region of the distribution is also where the forces are the most sensitive to image resolution, segmentation and thresholding. We believe a much higher spatial resolution is required before conclusions can be made about the precise shape of the force distribution in the region of low forces, in particular since the mean stress could not be adjusted.

The stress field in the pile is represented by a series of colour maps in Fig. 12 where each square is the cross section of a sub-volume of $4 \text{ mm} \times 4 \text{ mm} \times 12 \text{ mm}$. These sub-volumes contain ≈ 13 grains or ≈ 75 contacts which are used for stress calculations. These stress maps confirm a number of expected results. In the absence of any loading (stage 0), we observe a slight increase of the stress from top to bottom, in agreement with the fact that only the weight of the grains themselves acts at this stage. The same pattern is observed in all directions. The vertical component of the stress tensor shows an increase with the loading, as well as the radial and azimuthal components. The magnitude of the vertical component is about twice as large as the other two. Another finding of interest concerns the existence of the shear component (r, z). It is also notable that both vertical and radial components of the stress tensor have larger values near the boundary of the confining cylindrical cell at the 2nd stage of compression. Grains at the centre experience a reduced compression, due to their ability to move slightly towards the sides. Lateral grains are however under stronger radial and vertical displacement gradients. These maps are therefore in full agreement with the displacement field measured from the tracking of grains for high loadings (Fig. 8).

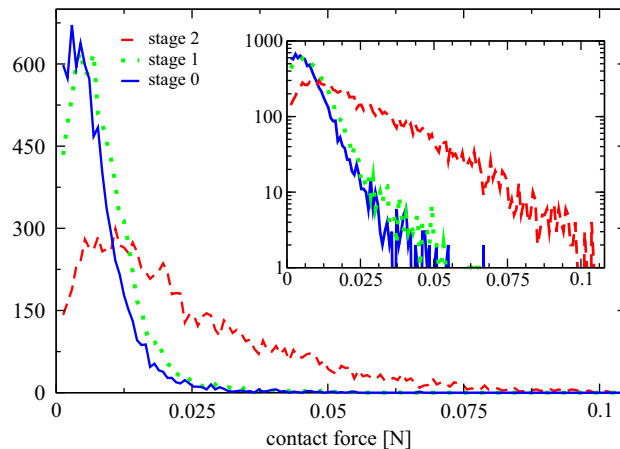


Fig. 11. Histograms of normal forces in the sample for all three loading stages.

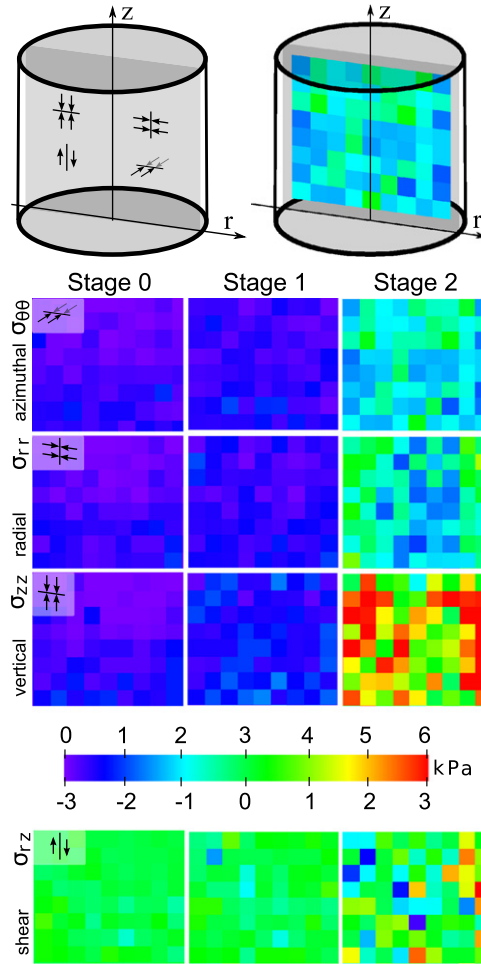


Fig. 12. Stress fields in a plane section of the sample for various loads. From top to bottom, (i) cartoons showing the location of the section in the sample, along a diameter, and various stress components reported, (ii) the stress map in the azimuthal direction $\sigma_{\theta\theta}$, in the radial direction σ_{rr} , in the vertical direction σ_{zz} , and shear stress σ_{rz} . The fluctuation in the stress maps is due to the limited number of contacts (≈ 75) in each sub-volumes δv .

4. Conclusion

We have presented in this paper the first measurements of internal stresses in a dry granular system resolved at the single grain scale. We have used here a simple geometry that allows us to calibrate and validate our measurements. In particular, we are now able to quantify, for the same pile, a number of characteristic features. They include mainly the evolution of the coordination number, the 2-point correlation function, the internal displacement fields, force distributions and stress fields, all as a function of loading. Taken together, all these measurements will enable us to better unravel the micromechanical behaviour of granular systems, in particular in quasistatic regimes. It is worth pointing out as well that by measuring the force based on the contact geometry, we are able to deal with non-symmetric and polydisperse grains.

Although we have proven that these measurements are realistic and achievable, a number of improvements are still required in order to study more complex cases. We need in particular to increase both the spatial statistics (number of grains) and the resolution at the contact scale; this will provide a better calibration of contact area extraction and therefore a more accurate measurement of forces and stress tensors within the pile. Increased image resolution will as a result improve the quantification of the coordination number and other geometric quantities and allow the use of stiffer grains and smaller loads, therefore widening the range of suitable materials to use for the grains. The accuracy of the force measurement can be further improved by refining the contact model to take into account tangential forces, that can be estimated from the orientation of the contact zone with respect to the centre-to-centre line. These technical advances, combined with the analysis tools presented here, will contribute to the understanding of a number of open problems. Internal force distribution can now be studied in the bulk, reaching the low force region of the distribution. The mechanics of the material and in particular its mechanical stability rely on the internal organisation of the grain contacts and also the force network. These are quantities that can be directly analysed in 3D, not only statically, but also dynamically by monitoring how an applied load affects each individual grain contact.

The kinematic study of the material can also be qualitatively and quantitatively extended. Not only the local strain can be measured, but the non-affine part of the displacement field is also directly accessible. The latter is increasingly thought to be related with the bulk material properties, in particular when the system is at the onset of rigidity (Wyart et al., 2008; Utter and Behringer, 2008). How such ideas can apply to 3D frictional granular systems remains to be investigated. In particular, answering such questions will require an extension to our current method so that we can study grain rotation. This would allow us to test the importance of micropolar elasticity in the mechanics of granular systems.

Acknowledgements

The authors wish to thank for the technical support of ANU's X-ray tomography team. We thank ANU Supercomputer Facility and NCI for their generous allocation of compute time. We also thank Ajay Limay and Jose Maorcio for assisting with some of the visualisations in this paper. M.S. acknowledges useful discussions with Nicolas Francois and Tomaso Aste. Financial support for this work through a grant from Australian Research Council, Project DP0881458, is gratefully acknowledged.

References

- Aste, T., Saadatfar, M., Senden, T.J., 2005. *Phys. Rev. E* 71 (6), 061302, doi:10.1103/PhysRevE.71.061302.
- Bernal, J.D., Mason, J., 1960. *Nature* 188, 910, doi:10.1038/188910a0.
- Blair, D.L., Mueggenburg, N.W., Marshall, A.H., Jaeger, H.M., Nagel, S.R., 2001. *Phys. Rev. E* 63 (4), 041304, doi:10.1103/PhysRevE.63.041304.
- Brockbank, R., Huntley, J.M., Ball, R.C., 1997. *J. Phys. I* 7 (10), 1521.
- Brujić, J., Edwards, S.F., Grinev, D.V., Hopkinson, I., Brujić, D., Makse, H.A., 2003. *Faraday Discuss.* 123, 207, doi:10.1039/b204414c.
- Brujić, J., Wang, P., Song, C., Johnson, D.L., Sindt, O., Makse, H.A., 2005. *Phys. Rev. Lett.* 95 (12), 128001, doi:10.1103/PhysRevLett.95.128001.
- Coppersmith, S.N., 1997. *Physica D: Nonlinear Phenom.* 107 (2–4), 183 16th Annual International Conference of the Center for Nonlinear Studies.
- Coppersmith, S.N., Liu, C.h., Majumdar, S., Narayan, O., Witten, T.A., 1996. *Phys. Rev. E* 53 (5), 4673, doi:10.1103/PhysRevE.53.4673.
- Corwin, E.I., Jaeger, H.M., Nagel, S.R., 2005. *Nature* 435 (7045), 1075.
- Dijksman, A.J., van Hecke, M., 2010. *Soft Matter* 6 (13), 2901, doi:10.1039/b925110c.
- Drescher, A., de Josselin de Jong, G., 1972. *J. Mech. Phys. Solids* 20 (5), 337, doi:10.1016/0022-5096(72)90029-4.
- Falk, M., Langer, J., 1998. *Phys. Rev. E* 57 (6), 7192.
- Feldkamp, L.A., Davis, L.C., Kress, J.W., 1984. *J. Opt. Soc. Am. A* 1, 612.
- Hertz, H., 1882. *J. Reine Angew. Math.* 92, 156.
- Howell, D., Behringer, R.P., Veje, C., 1999. *Phys. Rev. Lett.* 82 (26), 5241, doi:10.1103/PhysRevLett.82.5241.
- Janssen, H.A., 1895. *Z. Ver. Dtsch. Ing.* 39 (35), 1045.
- Johnson, K.L., 1987. *Contact Mechanics*. Cambridge University Press ISBN-13: 978-0521347969.
- Kabla, A.J., Senden, T.J., 2009. *Phys. Rev. Lett.* 102 (22), 228301, doi:10.1103/PhysRevLett.102.228301.
- Kabla, A., Debregeas, G., di Meglio, J.M., Senden, T.J., 2005. *Europhys. Lett.* 71 (6), 932.
- Kolb, E., Cviklinski, J., Lanuza, J., Claudin, P., Clément, E., 2004. *Phys. Rev. E* 69 (3), 031306, doi:10.1103/PhysRevE.69.031306.
- Langer, S.A., Liu, A.J., 2000. *Europhys. Lett.* 49 (1), 68.
- Lemaître, A., 2002. *Phys. Rev. Lett.* 89 (6), 64303.
- Liu, C.h., Nagel, S.R., Schecter, D.A., Coppersmith, S.N., Majumdar, S., Narayan, O., Witten, T.A., 1995. *Science* 269, 513, doi:10.1126/science.269.5223.513.
- Lois, G., Carlson, J.M., 2007. *Europhys. Lett.* 80, 5800, doi:10.1209/0295-5075/80/58001.
- Majumdar, S., Behringer, R.P., 2005. *Nature* 435, 1079, doi:10.1038/nature03805.
- Makse, H.A., Johnson, D.L., Schwartz, L.M., 2000. *Phys. Rev. Lett.* 84 (18), 4160, doi:10.1103/PhysRevLett.84.4160.
- Mantle, M.D., Sederman, A.J., Gladden, L.F., 2001. *Chem. Eng. Sci.* 56 (2), 523, doi:10.1016/S0009-2509(00)00256-6.
- Marmottant, A., Salvo, L., Martin, C., Mortensen, A., 2008. *J. Eur. Ceram. Soc.* 28 (13), 2441.
- Martin, C., Bordia, R., 2008. *Phys. Rev. E* 77 (3), 031307.
- Mindlin, R., 1949. *Trans. ASME* 71, A.
- Mueth, D.M., Jaeger, H.M., Nagel, S.R., 1998. *Phys. Rev. E* 57 (3), 3164, doi:10.1103/PhysRevE.57.3164.
- O'Hern, C.S., Langer, S.A., Liu, A.J., Nagel, S.R., 2001. *Phys. Rev. Lett.* 86 (1), 111, doi:10.1103/PhysRevLett.86.111.
- Radjai, F., Jean, M., Moreau, J., Roux, S., 1996. *Phys. Rev. Lett.* 77, 274.
- Saadatfar, M., 2006. *Morphological and Mechanical Characterisation of Microstructured Materials*. Ph.D. Thesis, The Australian National University.
- Saadatfar, M., Sheppard, A., Knackstedt, M.A., 2006. *Advances in X-ray Tomography for Geomaterials*, ISBN 1-905209-60-6, p. 269.
- Sakellariou, A., Sawkins, T.J., Senden, T.J., Limaye, A., 2004a. *Physica A* 339, 152.
- Sakellariou, A., Senden, T.J., Sawkins, T.J., Knackstedt, M.A., Turner, M.L., Jones, A.C., Saadatfar, M., Roberts, R.J., Limaye, A., Arns, C.H., Sheppard, A.P., Sok, R.M., 2004b. In: *SPIE Annual Meeting 2004*, August.
- Sheppard, A.P., Sok, R.M., Averdunk, H., 2004. *Physica A* 339, 145.
- Silbert, L.E., Ertas, D., Grest, G.S., Halsey, T.C., Levine, D., 2002. *Phys. Rev. E* 65, 031304.
- Soille, P., 2003. *Morphological Image Analysis: Principles and Applications*. Springer-Verlag ISBN:3540429883.
- Thornton, C., Antony, S., 1998. *Philos. Trans. Math. Phys. Eng. Sci.* 356 (1747), 2763.
- Utter, B., Behringer, R., 2008. *Phys. Rev. Lett.* 100 (20), 208302.
- Vincent, L., Soille, P., 1991. *IEEE Trans. Pattern Anal. Mach. Intell.* 13, 583.
- Weaire, D., Barry, J.D., Hutzler, S., 2010. *J. Phys.: Condens. Matter* 22 (19), 193101.
- Wyart, M., Liang, H., Kabla, A., Mahadevan, L., 2008. *Phys. Rev. Lett.* 101 (21), 215501, doi:10.1103/PhysRevLett.101.215501.
- Zhang, H.P., Makse, H.A., 2005. *Phys. Rev. E* 72 (1), 011301, doi:10.1103/PhysRevE.72.011301.
- Zhang, J., Majumdar, T., Tordesillas, A., Behringer, R., 2010. *Granular Matter* 12 (2), 159.
- Zhou, J., Long, S., Wang, Q., Dinsmore, A.D., 2006. *Science* 312 (5780), 1631, doi:10.1126/science.1125151.